Letter

Zirconia-Supported ZnO Single Layer for Syngas Conversion Revealed from Machine-Learning Atomic Simulation

Siyue Chen, Sicong Ma, and Zhi-Pan Liu*

Cite This: *J. Phys. Chem. Lett.* 2021, 12, 3328–3334

Read Online

ACCESS | 📊 Metrics & More | 📄 Article Recommendations | 🆂🅸 Supporting Information

ABSTRACT: ZnZrO ternary oxide represents a prominent catalytic system, identified recently for syngas conversion and CO_2 reduction via OX-ZEO technology. One intriguing observation of the ZnZrO catalyst is the very low amount of Zn required for achieving high activity, which challenges the current views on the active site of binary oxide catalysts. Herein, we demonstrate, via machine-learning-based atomic simulation, that the structure evolution of the ZnZrO system in synthesis can be traced from bulk to surface, which leads to the identification of the active site of the ZnZrO catalyst. Theory shows that an unprecedented single-layer Zn−O structure can adhere strongly to the monoclinic ZrO_2 minority (001) surface, forming a stable oxide-on-oxide interface Zn−O/M(001). The single-layer Zn−O can convert syngas to methanol with a high turnover frequency (7.38 s^{-1}) from microkinetics simulation. Electron structure analyses reveal that the pentahedron $[ZnO_4]$ in Zn−O/M(001) enhances the surface electron donation to promote the catalytic activity.
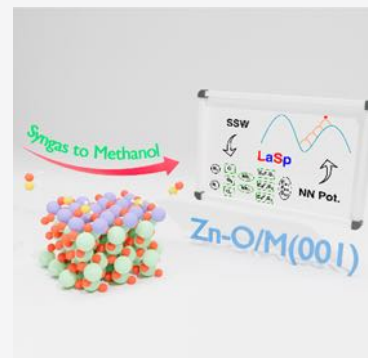
Significant recent efforts have been devoted to finding stable and active catalysts operating at high temperatures for syngas conversion (e.g., 673 K), which, when assembled with zeolite catalysts (the so-called OX-ZEO technology), allows for the one-step selective conversion of syngas to a variety of high-carbon-weight chemicals (e.g., olefins, ethanol, aromatics).[1] While many Zn-based oxides (ZnCrO, ZnZrO, ZnInO, ZnAlO, ZnGaO, etc.) were applied, among them, the ZnZrO system holds great promise for its nontoxicity, long-term durability, and good selectivity to olefin and aromatics.[2−12] However, because of the low Zn content in active ZnZrO catalysts and the high-temperature reaction conditions,[3−5] many fundamental questions for this system still remain open; the most pressing questions include the following: (i) Where does Zn reside in the catalyst? (ii) How does Zn participate in the CO/H_2 activation and affect the selectivity? New methods are called for to determine the active site and to clarify the reaction mechanism.

An important observation for the ZnZrO catalyst is that the Zn content (Zn%) can be as low as 1/200 in active catalysts,[5] which is considerably lower than that of other Zn-based oxide catalysts, such as CnZnO and ZnCrO catalysts (e.g., Zn:Cr = ~1:1 in the ZnCrO system).[13−15] The Wang group showed that pure ZrO_2/SSZ-13 yields a very low activity (<5% conversion rate), but with only 1.5% Zn addition, the activity is boosted to be over 20%. Upon further increase of the Zn% to 5.9%, the CO conversion reaches to 29% with the selectivity being 77% toward olefin.[4] These experiments imply that even a minority presence of Zn could be enough for CO/H_2 activation.

It is therefore of significance to clarify the atomic structure and the chemistry of Zn element in ZnZrO catalysts. Indeed,

ZnZrO catalysts with different Zn% has been characterized extensively in experiment, where the ZnO crystal (hexagonal phase) can be detected by X-ray powder diffraction (XRD) only above the Zn% of 50%.[3−5,7−10,16−18] This evidence suggests that the active Zn component is either distributed as extremely small clusters on ZrO_2 surface or dissolved into ZrO_2 lattice forming solid-solution, thus being difficult to detect by XRD. The former implication seems to be better supported by other experiments. For example, (i) X-ray photoelectron spectroscopy (XPS) analysis found that Zn is enriched two-fold in the surface region.[7] (ii) High-resolution transmission electron microscopy (HRTEM) starts to indicate individual lattice fringes of isolated ZnO, even at a 1% Zn content,[5] which reflects the difficulty of Zn cation presence inside ZrO_2. On the other hand, theoretical studies presented by the Li group proposed a simple solid-solution ZnZrO model, with on-site replacement surface Zr ions by Zn ions on the t-ZrO_2(101) surface. Their density function theory (DFT) calculations showed that the surface solid solution model can promote H_2 and CO_2 adsorption; therefore, the CO_2 hydrogenation can occur at the sites neighboring Zn and Zr sites.[7]

With state-of-the-art machine-learning-based atomic simulation we now resolve the active site of the ZnZrO system and
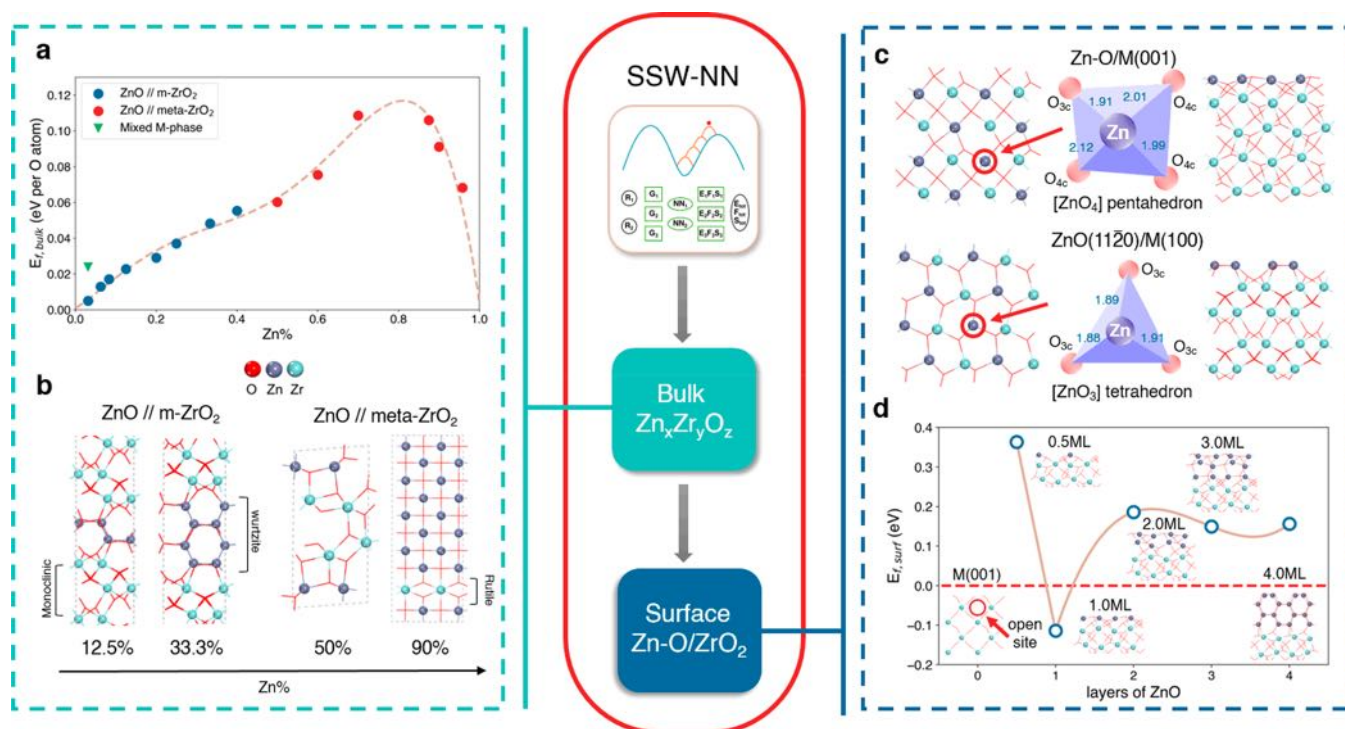
Figure 1. Thermodynamics of ZnZrO bulk phase and stable Zn−O overlayer structures on ZrO_2 surfaces revealed by SSW-NN simulation. (a) Thermodynamic phase diagram of ZnZrO. The blue and red circles represent the GM structures, and the green triangle represents the most stable solid-solution structure. (b) Four GM structures under the Zn content (Zn%) of 1/8, 1/3, 1/2, and 9/10, being either ZnO//m-ZrO_2 or ZnO//meta-ZrO_2 biphase structures, where the common bulk phase structures, such as monoclinic, wurtzite, and rutile, are denoted. (C) Two most stable Zn−O/ZrO_2 overlayer structures: Zn−O/M(001) and ZnO(11$\bar{2}$0)/M(100). The coordination of surface Zn atoms on both surfaces is highlighted, $[ZnO_4]$ pentahedron and $[ZnO_3]$ tetrahedron. (d) Formation energy ($E_{f,surf}$) of Zn−O on M(001) versus the thickness of ZnO. The insets show the structures, and the arrow in pristine M(001) indicates where Zn atoms locate.

quantify its activity. To allow for an efficient phase space exploration, we develop the first global neural network (G-NN) potential for the Zn−Zr−O ternary system that was automatically built upon the global potential energy surface (PES) of various bulk and surface samples as implemented in the stochastic surface walking (SSW) global optimization with neural network potential (SSW-NN) framework.[19−23] By evaluating the thermodynamic stability at reaction conditions, interestingly, the active site of the ZnZrO system was found to be a ZrO_2-supported Zn−O single-layer (Zn−O/ZrO_2) structure with $[ZnO_4]$ pentahedron coordination. The activity and selectivity of the ZnO−ZrO_2 interface were further verified by mapping out the lowest-energy reaction route and performing microkinetics simulations. Our theory reveals that ZnZrO is a new type of syngas conversion catalyst, i.e., oxide-on-oxide, different from conventional ZnCrO (oxide solid-solution) and CuZnO (metal-on-oxide) catalysts.

The theoretical methods utilized in this work are detailed in the Supporting Information (Methods and Table S1) and have been introduced and utilized in our previous work.[19−23] Here we emphasize that a reliable G-NN potential of the Zn−Zr−O ternary system is the key for the global PES exploration, which provides the high efficiency and accuracy of the PES evaluation. With the low-energy structural candidate obtained from SSW-NN, DFT calculations have been utilized to further verify all the key results at the final stage, with the benchmark between G-NN calculations and DFT calculations (see Table S2). Unless stated otherwise, all energetics data reported in this work are from DFT calculations using the generalized gradient approximation exchange−correlation functional at the level of

Perdew−Burke−Ernzerhof (GGA-PBE) with VASP software.[24−26] We have also considered the van der Waals correction (vdW) by the DFT-D3 method[27,28] for computing the reaction profile, which is found to be critical to obtain a more accurate reaction rate.

To determine the structure of the ZnZrO catalyst, herein we adopt a bottom-up approach by exploring the structural phase space of ternary ZnZrO materials starting from a random mixture of three elements and proceeding from bulk to surface guided by thermodynamics, as schematically shown in Figure 1.

More than 200 000 structure configurations with different Zn% in the ZnZrO ternary system have been visited by SSW-NN, based on which the bulk global minimum (GM) at different compositions is obtained. Figure 1a shows the bulk phase energy diagram of ZnZrO at Zn% from 1/32 to 0.96, where the formation energy $E_{f,bulk}$ of ZnZrO is referred to bulk ZnO wurtzite ($P6_3mc$, no.186) and ZrO_2 monoclinic phase (m-ZrO_2, $P2_1/c$, no.14). In the figure, the GMs are represented by circle points, which can be generally classified as two types of structures: (i) for Zn% < 0.4 (blue circles), GMs generally adopt the interface structure between ZnO and m-ZrO_2; (ii) for Zn% > 0.4 (red circles), GMs prefer an elongated lattice with the interface between ZnO and metastable ZrO_2 (e.g., rutile ZrO_2). Both are shown in Figure 1b.

Importantly, we found that the bulk structures of ZnZrO, irrespective of Zn%, are always less stable than individual m-ZrO_2 and ZnO, as reflected by the generally positive $E_{f,bulk}$ (see Table S3 for details). This result indicates that ZnZrO prefers

to segregate to ZnO and ZrO_2 phases instead of forming a single-crystal phase (oxide solid solution). As a result, the GM structures are always predicted to be biphase crystals between ZnO and ZrO_2 phases. These structures are increasingly unstable with the increase of Zn% (from 0 to 80%), apparently because monoclinic ZrO_2 can no longer be stable in the ZnO matrix (see Figure 1a,b). In fact, we note that the homogeneous solid-solution phase never occurs to be GM for all Zn% investigated as they are even more unstable than the biphases, e.g., 1/32 Zn in m-ZrO_2 (green triangle in Figure 1a) and 1/5 Zn in tetragonal ZrO_2 (t-ZrO_2). The $E_{f,bulk}$ of 1/32 Zn in m-ZrO_2 is 18.8 meV per O atom higher than the GM. More details on the bulk phases can be found in Figures S1 and S2 and Table S4.

We found that the biphase GM structures for Zn% < 40% share the same orientation relationship (OR) between hexagonal ZnO and m-ZrO_2, that is, ZnO(11$\bar{2}$0)//m-ZrO_2(100), ZnO[0001]//m-ZrO_2[001], as shown in Figure 1b. This interfacial phase can achieve a good structure match in both lattice (strain <2% for ZnO and <1% for m-ZrO_2) and atoms. The interfacial O atoms can maintain the same coordination number with cations (Zn + Zr) as they are in the individual bulk (Zn or Zr). The presence of the coherent biphase junction suggests an alternative mode for Zn coexistence with ZrO_2; that is, ZnO may disperse uniformly on ZrO_2 surfaces and form interface oxide-on-oxide structures. This inspires us to explore the possible thin surface phases for ZnO-ZrO_2.

Next, we searched the stable composite surfaces with Zn−O overlayers growing on exposed ZrO_2 surfaces (Zn−O/ZrO_2). Nine low Miller index surfaces of two common ZrO_2 phases, monoclinic (M) and tetragonal (T) phases, were considered, including M(100), M(001), M(111), M($\bar{1}$11), M(011), T(101), T(100), T(111), and T(001). For each surface, the final surface configuration was determined from more than 10 000 local minima visited by the SSW-NN method. Two quantitative criteria are utilized in evaluating the stability, $E_{f,surf}$ defined in eq 1, and γ_ZnZrO defined in eq 2, where E_{slab} is the energy of the surface slab in modeling surface and E_{bulk} is the energy of the bulk oxide. $E_{f,surf}$ thus reflects the segregation tendency of Zn−O overlayer on ZrO_2 surface, whereas γ_ZnZrO quantifies the stability of the surface.

$$E_{f,surf} = (E_{slab(ZnZrO)} - N_{Zn}E_{bulk(ZnO)} - E_{slab(ZrO_2)})/N_{Zn} \quad (1)$$

$$\gamma\text{_ZnZrO} = (E_{slab(ZnZrO)} - N_{Zn}E_{bulk(ZnO)} - N_{Zr}E_{bulk(ZrO_2)})/(2A_{surf}) \quad (2)$$

We found that only three surfaces can form stable Zn−O overlayers, as listed in Table 1, i.e., M(001), M(100), and T(111), which have negative $E_{f,surf}$ (details for the other positive $E_{f,surf}$ structures are reported in Figure S3 and Table S5). These three ZrO_2 surfaces have relatively high surface

Table 1. Energetics for Three Stable ZnO Overlayers on ZrO_2 Surfaces[a]

surface	Zn−O/A_{Surf} (mmol/m^2)	$E_{f,surf}$ (eV)	γ_ZnZrO (J/m^2)
M(001)	0.440	−0.111	1.271
M(100)	0.427	−0.139	1.314
T(111)	0.369	−0.032	1.114

[a]Listed data include the concentration of surface Zn−O (Zn−O/A_{surf}), the formation energy ($E_{f,surf}$), and the surface energy (γ_ZnZrO).

energies (γ_ZrO_2 = 1.401, 1.472, and 1.145 J/m^2 for M(001), M(100), and T(111), respectively) with less coordinated surface Zr and O atoms, which are the key for them to adhere the Zn−O overlayer. In particular, the $E_{f,surf}$ values of Zn−O overlayer on m-ZrO_2(001) and (100) are lower, being −0.139 and −0.111 eV. In contrast, for the most stable surfaces of m-ZrO_2, M($\bar{1}$11) and M(111) (γ_ZrO_2 = 0.864 and 1.046 J/m^2, respectively), their surface atoms are close to coordination saturation, and thus, the addition of the Zn−O overlayer is highly endothermic (positive $E_{f,surf}$). Obviously, the minority surfaces of ZrO_2 can be stabilized in the presence of Zn, which become energetically competitive with the majority ones. It might be mentioned that the growth mode for the Zn−O overlayer on M(100) follows exactly the biphase junction OR in the bulk GM below 40% Zn content, as shown in Figure 1c. In other words, the ZnO overlayer on M(100) is structurally similar to that of ZnO(11$\bar{2}$0). Because of the good lattice match, ZnO(11$\bar{2}$0)/M(100) is expected to be a dominant growth mode for large ZnO particles anchoring on ZrO_2.

Among the three thermodynamically allowed Zn−O overlayer structures (Table 1), we choose Zn−O/M(001) as the first candidate for the active site of syngas conversion because (i) the Zn−O layer is more stable on m-ZrO_2 surfaces ($E_{f,surf}$ ←0.1 eV) than it is on the t-ZrO_2 surface ($E_{f,surf}$ = −0.032 eV) and (ii) M(001) has a lower surface energy than M(100), while the Zn−O layer on M(001) also presents a lower surface energy than on (100), which suggests that Zn will have a higher concentration on M(001). In addition, the Zn−O/M(001) has the highest concentration of Zn−O (0.440 mmol/m^2) among three stable overlayer structures, indicating that M(001) can better accumulate Zn−O species.

Figure 1c highlights the atomic structure of Zn−O/M(001). For M(001), it is a rugged surface with equal numbers of exposed five-coordinate Zr (Zr$_{5c}$) and six-coordinate Zr (Zr$_{6c}$) that are linked by two-coordinate O (O$_{2c}$). Because of the presence of open sites (see arrows in Figure 1d inset) near surface Zr$_{5c}$, extra Zn cations and O anions of Zn−O overlayer can fill into these positions, forming a linear chain of −[Zn−O]− along the [110] direction, where each Zn features a unique [ZnO$_4$] pentahedron structure, as highlighted in Figure 1c, whereas the O atoms are O$_{3c}$ and O$_{4c}$ in alternation. By comparison with common surfaces of ZnO, we found that the atomic arrangement of this Zn−O overlayer does not resemble any known ZnO surfaces, which implies the new chemistry of Zn−O/M(001). After the addition of Zn−O overlayer on M(001), all unsaturated surface Zr atoms become Zr$_{7c}$ and the original O$_{2c}$ also reaches to the saturated bulk state as O$_{4c}$. Apparently, the Zn−O layer smooths the pristine M(001) and leads to a flat geometry of Zn−O/M(001). Not surprisingly, when further adding or reducing Zn−O layers on M(001) (see Figure 1d), the formed multilayer structures turn out to be thermodynamically less stable. This suggests that the single layer is also kinetically stable and thus can be a good candidate for high-temperature catalysis.

We are now in a position to examine the catalytic performance of syngas conversion on Zn−O/M(001). Because the reaction occurs under high temperatures (e.g., 673 K) and reductive gas (H$_2$), the thermodynamics analysis is performed on Zn−O/M(001) surface to inspect the possibility of oxygen vacancy (O$_v$) exposure. Our results show that the surface is reluctant to produce O$_v$ in the presence of H$_2$ because of the high stability of the surface Zn−O structure). The O$_v$
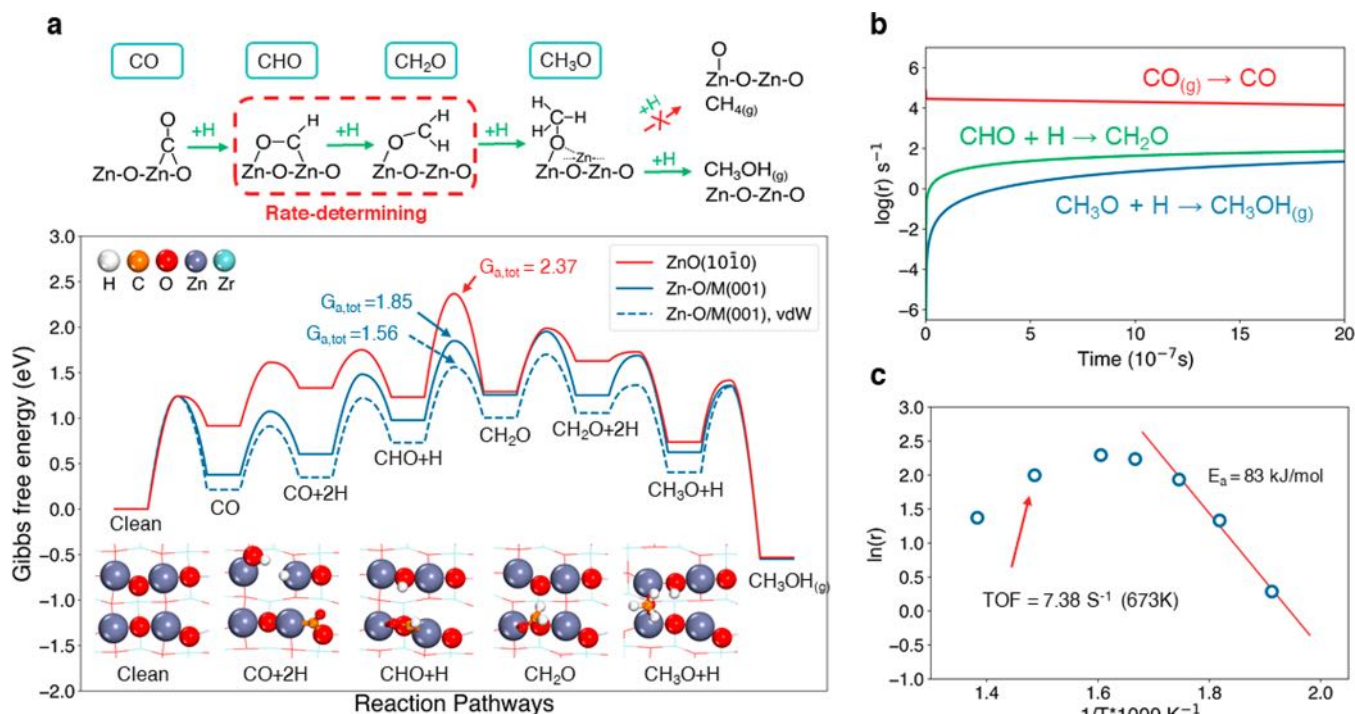
Figure 2. Reaction mechanisms for syngas conversion. (a) Gibbs free energy profile of syngas conversion on Zn−O/M(001) and ZnO(10$\bar{1}$0) at 673 K and 3 MPa (H$_2$:CO = 2:1). The key reaction intermediates on Zn−O/M(001) and the mechanism are also depicted. The solid lines are from DFT/GGA-PBE results, and the dotted line has the vdW correction. (b) Reaction rates from microkinetics simulation for syngas conversion on Zn−O/M(001), including the rate of CO consumption, CH$_3$OH production, and the rate-determining step (hydrogenation from CHO to CH$_2$O). (c) The plot for overall reaction rate versus temperature using the DFT/GGA-PBE energetics with vdW correction, from which the apparent activation energy is fitted in the 523−573 K window.

generation is endothermic at H$_2$ pressure of 2 atm until the temperature is greater than 800 K. This is also true at the syngas conversion condition (CO and H$_2$ coexistence, see Figure S4 and Table S6).

On the stoichiometric Zn−O/M(001) surface, we then investigated the possible reaction pathways using DFT calculation. The results are compared with those on ZnO(10$\bar{1}$0), the dominant surface of ZnO particles.[29] The lowest-energy pathway of syngas conversion to methanol is summarized in Figure 2a, which contains the Gibbs free energy reaction profiles together with the reaction snapshots of key intermediates. When computing the free energy profile, the reaction condition is set to 673k, 3 MPa, and H$_2$:CO = 2:1, typically used in experiment. As shown in Figure 2a, while the syngas conversion on Zn−O/M(001) and ZnO(10$\bar{1}$0) follow the same reaction mechanism, i.e. via the stepwise hydrogenation pathway mediated by CHO, CH$_2$O and CH$_3$O (CO → CHO → CH$_2$O → CH$_3$O → CH$_3$OH), the reaction on Zn−O/M(001) is remarkably more facile than that on ZnO(10$\bar{1}$0).

Taking the reaction on Zn−O/M(001) as an example, the reaction starts by CO adsorption on the exposed Zn$_{4c}$ (pentahedron Zn) and H$_2$ dissociative adsorption on a nearby Zn−O pair (denoted as CO+2H state in Figure 2a). While the adsorptions of CO and H$_2$ are exothermic in energy (E_{ads} = −0.97 eV for CO and −0.67 eV for H$_2$), they are highly endothermic at 673 K reaction conditions because of the large entropy loss of the gas-phase molecule (+1.20 eV for CO and +0.70 eV for H$_2$) in adsorption. It is worth mentioning that there are several possible adsorption structures for both CO and the dissociated H (detailed in Figure S5), and these

configurations can transform between each other facilely (E_a < 0.2 eV). Only the most stable configurations are reported in the energy profile.

The hydride (H bonding with Zn cation) will react first with nearby CO by overcoming a barrier of 0.88 eV. This step ends up with a bidentated CHO intermediate with its C and O linking with two surface Zn cations by releasing 0.50 eV. Subsequently, the other proton H (H bonding with O anion) will attack this CHO to produce formaldehyde CH$_2$O intermediate with a barrier of 0.87 eV, which dictates the highest-energy position in the reaction profile. The obtained formaldehyde can either desorb with a cost of 0.43 eV or react with another pair of H atoms that dissociate nearby. Further hydrogenation of CH$_2$O to CH$_3$O is highly exothermic (−1.06 eV), occurring with a low energy barrier (0.44 eV). The nascent CH$_3$O bonds with two neighboring Zn cations with its O atom. Finally, CH$_3$O can be hydrogenated by the remaining proton (H on O$_{3c}$) to produce CH$_3$OH that then desorbs by overcoming a barrier of 0.74 eV.

We emphasize that the production of CH$_4$ by CH$_3$O+H → CH$_4$+O is kinetically inhibited on Zn−O/M(001), because the barrier is more than 3.5 eV. This is because the additional O produced is unable to adsorb on the stoichiometric Zn−O/ZrO$_2$ surface (endothermic by 1.57 eV with respect to the gas-phase O$_2$). On the other hand, our previous study on ZnCrO catalyst shows that the CH$_4$ production becomes competitive when the O$_v$ generation is facile and the surface can undergo the redox transformation by creating/healing O$_v$ during the reaction. However, the same picture does not apply to the ZnZrO system, where the O$_v$ formation is at least 0.71 eV

(3.37 vs 2.66 eV with respect to 1/2 gas-phase O_2) more difficult than that of the $ZnCr_2O_4$ surface.[13]

In contrast, the reaction from syngas to methanol on $ZnO(10\bar{1}0)$ is much more difficult to accomplish (also shown in Figure 2a). We note that the major difference lies in the stability of intermediates, including CO, H, and CHO species, all of which can adopt a more stable configuration on Zn−O/M(001). Consistently, the TS of CHO hydrogenation is also more stable on Zn−O/M(001). As a result, the overall barrier of Zn−O/M(001) is significantly lower than that of $ZnO(10\bar{1}0)$. Notably, the CHO adsorption geometries on Zn−O/M(001) and on $ZnO(10\bar{1}0)$ are in fact similar (depicted in Figure S8): the C and O of CHO bond with two neighboring Zn. This implies that the special electronic structure of the Zn−O layer on ZrO_2 is the key factor that allows syngas conversion to methanol on ZnZrO.

The overall free energy barrier ($G_{a,tot}$) of syngas conversion on Zn−O/M(001) is 1.85 eV (GGA-PBE functional, see Figure 2a), which is the energy difference between the surface TS of CH_2O formation and the gas-phase molecules, while that for $ZnO(10\bar{1}0)$ is much higher (2.37 eV). Considering the overall barrier is not determined by the surface reaction in the Langmuir−Hinshelwood mechanism but more like a reaction in the Eley−Rideal mechanism, we have also applied the vdW correction (DFT-D3)[27,28] to the reaction profile. After vdW correction, the overall barrier is found to decrease to 1.56 eV on Zn−O/M(001) and to 2.10 eV on $ZnO(10\bar{1}0)$. The vdw-corrected profile on Zn−O/M(001) is also shown in Figure 2a, which is found to affect quite consistently for most surface-adsorbed states (stabilizing the states by 0.2−0.3 eV).

To establish the reaction kinetics and compare with experimental data, we performed microkinetics simulation at a series of temperatures to determine the turnover frequency (TOF) and fit the apparent activation energy. We have performed microkinetics simulation using the reaction data with and without of the vdW correction (all data are listed Tables S7−S9). Figure 2b shows the time-resolved rate including CO consumption, CH_3OH production, and the hydrogenation from CHO to CH_2O under 673 K. The hydrogenation from CHO to CH_2O appears to be the rate-determining step, which is consistent with the energy profile in Figure 2a. The calculated TOF of CH_3OH production under 673 K is 0.09 and 7.38 s^{-1} without and with vdW correction, respectively (shown in Figure 2c), equivalent to the logarithm of consumption rate of CO ($\ln(r_{CO})$) at −3.32 and 1.08 mmol $g^{-1} h^{-1}$, respectively (see Methods for the estimation). The apparent energy barrier (E_a) within the linear range of 523−573 K yields a value of 83 kJ/mol, as shown in the fitted line in Figure 2c. While the TOF without vdW correction is too low, our kinetics data from vdW-corrected energy profile are well consistent with the experimental values, i.e., ∼1.20 mmol $g^{-1} h^{-1}$ CO consumption rate for ZnZrO (Zn% = 1/16) catalyst and 72 ± 5 kJ/mol for the apparent activation energy.[4]

It is of interest to discuss why the vdw correction is critical for Zn−O/ZrO_2 catalysis. Apparently, there are two causes. First, the reaction occurs at high temperatures (673 K), where the gas-phase molecule adsorption becomes endothermic because of the loss of entropy. Second, the key intermediates (e.g., CHO) generally have a low adsorption ability on the oxide surface that leads to the overall barrier being determined by a surface TS and the initial state of the gas-phase molecules. In this case, the intrinsic DFT error cannot be well canceled

out, and thus, vdW correction for adsorbed states turns out to be important.

In order to understand the enhanced intermediate stability on Zn−O/M(001), we performed the electronic structure analysis for the two surfaces (Zn−O/M(001) and $ZnO(10\bar{1}0)$) with and without adsorption of CHO. The Bader charge analysis shows that on both surfaces, the adsorbed CHO species is negatively charged by ∼0.5|e| that accumulate mainly on the C and O ends (see data in Figure S6 and Table S10). This result indicates that a good catalyst needs to act as an efficient electron donor in order to bond CHO strongly. By projecting the density of states (pDOS) onto the surface Zn and O valence states, i.e., Zn 3d and O 2p orbitals displayed in Figure 3a and Figure S7, respectively, we found
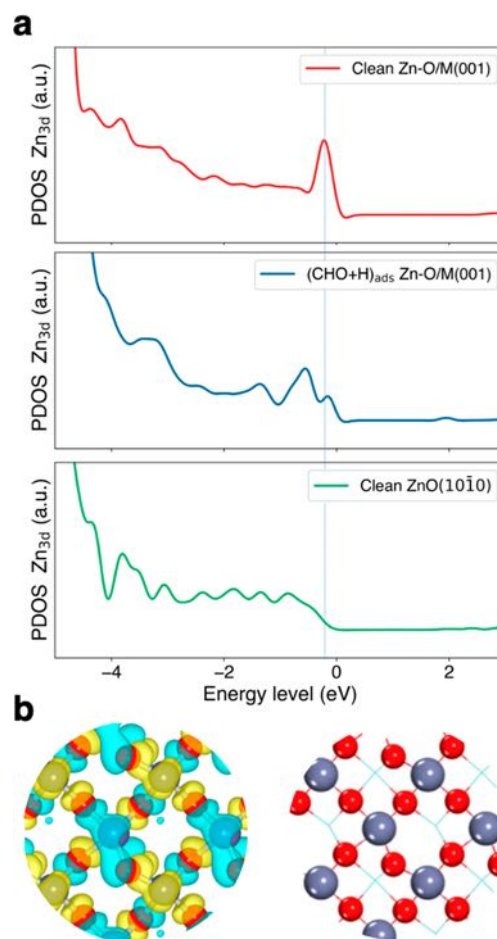

Figure 3. Electronic structure reveals the origin for the catalytic activity of Zn−O/M(001). (a) Projected DOS onto the surface Zn 3d orbital for the clean Zn−O/M(001) surface, CHO adsorbed Zn−O/M(001) and the clean $ZnO(10\bar{1}0)$ surface. (b) Wave function contour plot of the VBM state (left) in the clean Zn−O/M(001) and the atomic structure (right). The 3D isosurface value is set as 0.002 e $Å^{-3}$.

that the highest occupied states do exhibit salient difference between Zn−O/M(001) and $ZnO(10\bar{1}0)$: For bare Zn−O/M(001) surface, both the Zn 3d states and O 2p states have the larger population (see Figures 3a and S7, respectively) just below the valence band maximum (VBM), indicating that the Zn−O/M(001) surface can better supply electrons and form bonding with coming species. The wave functions of the VBM state for Zn−O/M(001) and $ZnO(10\bar{1}0)$ are also plotted (in

Figures 3b and S8), showing that only the Zn on Zn−O/M(001) has significant electron distribution. Indeed, these high-energy Zn 3d states on Zn−O/M(001) evolve into the covalent bonding between the exposed Zn_{4c} and CHO group via the 3d−2p hybridization.

We thus can summarize that the Zn−O single layer on ZrO_2 is chemically active with better electron donating and covalent bonding ability, which is attributed to the fact that Zn on ZrO_2 is not in its conventional tetrahedron coordination, but a unique pentahedron geometry with Zn in four O coordination ($[ZnO_4]$ in Figure 1c). The open ZrO_2 surface sites help to stabilize these active surface Zn and O atoms by electrostatic interaction and afford them a higher covalent bonding ability.

By using machine-learning-based large-scale atomistic simulation, we discover an unprecedented Zn pentahedron bonding geometry that is present in the Zn−O single-layer stabilized by the ZrO_2 minority surface. This Zn−O single layer enables the high-temperature syngas conversion on the ZnZrO system by stabilizing the key reaction intermediate CHO species. Our results settle the puzzles on the nature of Zn in ZrO_2, by ruling out the possibility of forming solid-solution of Zn−Zr oxide and clarifying the high activity and selectivity using the Zn−O/M(001) composite. By comparison with the syngas conversion on the ZnCrO system (the reaction occurs on the $Zn_3Cr_3O_8$ crystal surfaces), the ZnZrO system exhibits a new type of catalysis for syngas conversion via an interface structure, where a small amount of Zn is enough to promote the whole catalysis. With all results learned here from first-principles data, from bulk phase diagram to surface stability and reactivity and kinetics, this work demonstrates the power of machine-learning potential in predicting complex catalysis and thus holds promise for full-cycle catalyst design in silico.

■ ASSOCIATED CONTENT

ⓈI Supporting Information

The Supporting Information is available free of charge at https://pubs.acs.org/doi/10.1021/acs.jpclett.1c00596.

    SSW-NN methodology and calculation details, covering the data benchmarking, the bulk and surface phases, Gibbs free energy profile and microkinetics simulation details, and Cartesian coordinates of Zn−O/M(001) and $ZnO(11\bar{2}0)/M(100)$ (PDF)

■ AUTHOR INFORMATION

Corresponding Author

Zhi-Pan Liu − *Collaborative Innovation Center of Chemistry for Energy Material, Shanghai Key Laboratory of Molecular Catalysis and Innovative Materials, Key Laboratory of Computational Physical Science, Department of Chemistry, Fudan University, Shanghai 200433, China;* ● orcid.org/0000-0002-2906-5217; Email: zpliu@fudan.edu.cn

Authors

Siyue Chen − *Collaborative Innovation Center of Chemistry for Energy Material, Shanghai Key Laboratory of Molecular Catalysis and Innovative Materials, Key Laboratory of Computational Physical Science, Department of Chemistry, Fudan University, Shanghai 200433, China*

Sicong Ma − *Collaborative Innovation Center of Chemistry for Energy Material, Shanghai Key Laboratory of Molecular Catalysis and Innovative Materials, Key Laboratory of*

Computational Physical Science, Department of Chemistry, Fudan University, Shanghai 200433, China; ● orcid.org/0000-0001-5894-5910

Complete contact information is available at:
https://pubs.acs.org/10.1021/acs.jpclett.1c00596

Author Contributions

Z.-P.L. conceived the project and contributed to the design of calculations and the analyses of all data. S.M. carried out the training of G-NN potential and the electron structure analysis. S.C. accomplished most of the calculations and drafted the manuscript. All the authors have been engaged into the discussion of results and commenting on the manuscripts.

Notes

The authors declare no competing financial interest.
The software code of LASP and G-NN potential within the Letter is available from the corresponding author or the web site http://www.lasphub.com.

■ REFERENCES

(1) Jiao, F.; Li, J.; Pan, X.; Xiao, J.; Li, H.; Ma, H.; Wei, M.; Pan, Y.; Zhou, Z.; Li, M.; et al. Selective Conversion of Syngas to Light Olefins. *Science* **2016**, *351* (6277), 1065−1068.

(2) Zhou, W.; Cheng, K.; Kang, J.; Zhou, C.; Subramanian, V.; Zhang, Q.; Wang, Y. New Horizon in C1 Chemistry: Breaking the Selectivity Limitation in Transformation of Syngas and Hydrogenation of CO_2 into Hydrocarbon Chemicals and Fuels. *Chem. Soc. Rev.* **2019**, *48* (12), 3193−3228.

(3) Cheng, K.; Gu, B.; Liu, X.; Kang, J.; Zhang, Q.; Wang, Y. Direct and Highly Selective Conversion of Synthesis Gas into Lower Olefins: Design of a Bifunctional Catalyst Combining Methanol Synthesis and Carbon-Carbon Coupling. *Angew. Chem.* **2016**, *128* (15), 4803−4806.

(4) Liu, X.; Zhou, W.; Yang, Y.; Cheng, K.; Kang, J.; Zhang, L.; Zhang, G.; Min, X.; Zhang, Q.; Wang, Y. Design of Efficient Bifunctional Catalysts for Direct Conversion of Syngas into Lower Olefins *via* Methanol/Dimethyl Ether Intermediates. *Chem. Sci.* **2018**, *9* (20), 4708−4718.

(5) Cheng, K.; Zhou, W.; Kang, J.; He, S.; Shi, S.; Zhang, Q.; Pan, Y.; Wen, W.; Wang, Y. Bifunctional Catalysts for One-Step Conversion of Syngas into Aromatics with Excellent Selectivity and Stability. *Chem.* **2017**, *3* (2), 334−347.

(6) Kang, J.; He, S.; Zhou, W.; Shen, Z.; Li, Y.; Chen, M.; Zhang, Q.; Wang, Y. Single-Pass Transformation of Syngas into Ethanol with High Selectivity by Triple Tandem Catalysis. *Nat. Commun.* **2020**, *11* (1), 827.

(7) Wang, J.; Li, G.; Li, Z.; Tang, C.; Feng, Z.; An, H.; Liu, H.; Liu, T.; Li, C. A Highly Selective and Stable ZnO-ZrO_2 Solid Solution Catalyst for CO_2 Hydrogenation to Methanol. *Sci. Adv.* **2017**, *3* (10), No. e1701290.

(8) Zhou, C.; Shi, J.; Zhou, W.; Cheng, K.; Zhang, Q.; Kang, J.; Wang, Y. Highly Active ZnO-ZrO_2 Aerogels Integrated with H-ZSM-5 for Aromatics Synthesis from Carbon Dioxide. *ACS Catal.* **2019**, *10*, 302−310.

(9) Li, Z.; Qu, Y.; Wang, J.; Liu, H.; Li, M.; Miao, S.; Li, C. Highly Selective Conversion of Carbon Dioxide to Aromatics over Tandem Catalysts. *Joule* **2019**, *3* (2), 570−583.

(10) Li, Z.; Wang, J.; Qu, Y.; Liu, H.; Tang, C.; Miao, S.; Feng, Z.; An, H.; Li, C. Highly Selective Conversion of Carbon Dioxide to Lower Olefins. *ACS Catal.* **2017**, *7* (12), 8544−8548.

(11) Crisci, A. J.; Dou, H.; Prasomsri, T.; Román-Leshkov, Y. Cascade Reactions for the Continuous and Selective Production of Isobutene from Bioderived Acetic Acid Over Zinc-Zirconia Catalysts. *ACS Catal.* **2014**, *4* (11), 4196−4200.

(12) Dagle, V. L.; Dagle, R. A.; Kovarik, L.; Baddour, F.; Habas, S. E.; Elander, R. Single-step Conversion of Methyl Ethyl Ketone to Olefins over Zn$_x$Zr$_y$O$_z$ Catalysts in Water. *ChemCatChem* **2019**, *11* (15), 3393−3400.

(13) Ma, S.; Huang, S.-D.; Liu, Z.-P. Dynamic Coordination of Cations and Catalytic Selectivity on Zinc−Chromium Oxide Alloys during Syngas Conversion. *Nat. Catal* **2019**, *2*, 671.

(14) Molstad, M. C.; Dodge, B. F. Zinc Oxide−Chromium Oxide Catalysts for Methanol Synthesis. *Ind. Eng. Chem.* **1935**, *27* (2), 134−140.

(15) Behrens, M.; Studt, F.; Kasatkin, I.; Kuhl, S.; Havecker, M.; Abild-Pedersen, F.; Zander, S.; Girgsdies, F.; Kurr, P.; Kniep, B.-L.; Tovar, M.; Fischer, R. W.; Norskov, J. K.; Schlogl, R. The Active Site of Methanol Synthesis over Cu/ZnO/Al2O3 Industrial Catalysts. *Science* **2012**, *336* (6083), 893−897.

(16) Baylon, R. A. L.; Sun, J.; Kovarik, L.; Engelhard, M.; Li, H.; Winkelman, A. D.; Wang, Y. Structural Identification of ZnxZryOz Catalysts for Cascade Aldolization and Self-Deoxygenation Reactions. *Appl. Catal., B* **2018**, *234*, 337−346.

(17) Liu, C.; Sun, J.; Smith, C.; Wang, Y. A Study of ZnxZryOz Mixed Oxides for Direct Conversion of Ethanol to Isobutene. *Appl. Catal., A* **2013**, *467*, 91−97.

(18) Uribe López, M. C.; Alvarez Lemus, M. A.; Hidalgo, M. C.; López González, R.; Quintana Owen, P.; Oros-Ruiz, S.; Uribe López, S. A.; Acosta, J. Synthesis and Characterization of ZnO-ZrO$_2$ Nanocomposites for Photocatalytic Degradation and Mineralization of Phenol. *J. Nanomater.* **2019**, *2019*, 1−12.

(19) Huang, S.-D.; Shang, C.; Kang, P.-L.; Liu, Z.-P. Atomic Structure of Boron Resolved Using Machine Learning and Global Sampling. *Chem. Sci.* **2018**, *9* (46), 8644−8655.

(20) Behler, J.; Parrinello, M. Generalized Neural-Network Representation of High-Dimensional Potential-Energy Surfaces. *Phys. Rev. Lett.* **2007**, *98* (14), 146401.

(21) Huang, S.-D.; Shang, C.; Kang, P.-L.; Zhang, X.-J.; Liu, Z.-P. LASP: Fast Global Potential Energy Surface Exploration. *WIREs Comput. Mol. Sci.* **2019**, *9*, e1415 DOI: 10.1002/wcms.1415.

(22) Huang, S.-D.; Shang, C.; Zhang, X.-J.; Liu, Z.-P. Material Discovery by Combining Stochastic Surface Walking Global Optimization with a Neural Network. *Chem. Sci.* **2017**, *8* (9), 6327−6337.

(23) Kang, P.-L.; Shang, C.; Liu, Z.-P. Large-Scale Atomic Simulation via Machine Learning Potentials Constructed by Global Potential Energy Surface Exploration. *Acc. Chem. Res.* **2020**, *53* (10), 2119−2129.

(24) Kresse, G.; Joubert, D. From Ultrasoft Pseudopotentials to the Projector Augmented-Wave Method. *Phys. Rev. B: Condens. Matter Mater. Phys.* **1999**, *59* (3), 1758−1775.

(25) Blöchl, P. E. Projector Augmented-Wave Method. *Phys. Rev. B: Condens. Matter Mater. Phys.* **1994**, *50* (24), 17953−17979.

(26) Perdew, J. P.; Burke, K.; Ernzerhof, M. Generalized Gradient Approximation Made Simple. *Phys. Rev. Lett.* **1996**, *77* (18), 3865.

(27) Grimme, S.; Ehrlich, S.; Goerigk, L. Effect of the Damping Function in Dispersion Corrected Density Functional Theory. *J. Comput. Chem.* **2011**, *32* (7), 1456−1465.

(28) Grimme, S.; Antony, J.; Ehrlich, S.; Krieg, H. A Consistent and Accurate Ab Initio Parametrization of Density Functional Dispersion Correction (DFT-D) for the 94 Elements H-Pu. *J. Chem. Phys.* **2010**, *132*, 154104.

(29) Li, N.; Jiao, F.; Pan, X.; Ding, Y.; Feng, J.; Bao, X. Size Effects of ZnO Nanoparticles in Bifunctional Catalysts for Selective Syngas Conversion. *ACS Catal.* **2019**, *9* (2), 960−966.